HHS Public Access

Author manuscript

Glia. Author manuscript; available in PMC 2023 October 19.

Published in final edited form as:

Glia. 2021 December ; 69(12): 2981–2998. doi:10.1002/glia.24083.

H-ferritin expression in astrocytes is necessary for proper oligodendrocyte development and myelination

VT Cheli[*],

DA Santiago González[*],

Q Wan[*],

G Denaroso,

R Wan,

SL Rosenblum,

PM Paez

Institute for Myelin and Glia Exploration, Department of Pharmacology and Toxicology, Jacobs School of Medicine and Biomedical Sciences, The State University of New York, University at Buffalo, Buffalo, New York.

Abstract

How iron is delivered to the CNS for myelination is poorly understood. Astrocytes are the most abundant glial cells in the brain and are the only cells in close contact with blood vessels. Therefore, they are strategically located to obtain nutrients, such as iron, from circulating blood. To determine the importance of astrocyte iron uptake and storage in myelination and remyelination, we conditionally knocked-out the expression of the divalent metal transporter 1 (**DMT1**), the transferrin receptor 1 (**Tfr1**) and the ferritin heavy subunit (**Fth**) in Glast-1-positive astrocytes. DMT1 or Tfr1 ablation in astrocytes throughout early brain development did not significantly affects oligodendrocyte maturation or iron homeostasis. However, blocking Fth production in astrocytes during the first postnatal week drastically delayed oligodendrocyte development and myelin synthesis. Fth knockout animals presented an important decrease in the number of myelinating oligodendrocytes and a substantial reduction in the percentage of myelinated axons. This postnatal hypomyelination was accompanied by a decline in oligodendrocyte iron uptake and with an increase in brain oxidative stress. We also tested the relevance of astrocytic Fth expression in the cuprizone model of myelin damage and repair. Fth deletion in Glast1-positive astrocytes significantly reduced myelin production and the density of mature myelinating oligodendrocytes throughout the complete remyelination process. These results indicate that Fth iron storage in astrocytes is vital for early oligodendrocyte development as well as for the remyelination of the CNS.

Correspondence to: Pablo M. Paez, Institute for Myelin and Glia Exploration, Department of Pharmacology and Toxicology, Jacobs School of Medicine and Biomedical Sciences, SUNY at Buffalo. NYS Center of Excellence, 701 Ellicott St., Buffalo, New York 14203, USA. Tel: 716-881-7823; Fax: 716-849-6651; ppaez@buffalo.edu.

[*]These authors made equivalent contributions.

Conflict of interest statement: The authors declare no competing financial interests.

Keywords

astrocytes; iron; DMT1; ferritin; transferrin receptor; myelination; remyelination

INTRODUCTION

Astrocytes, the most abundant glial cells in the brain and spinal cord, exert many essential functions during development in both gray and white matter. For example, astrocytes play a primary role in synaptic transmission and information processing in neural circuits (Christopherson et al., 2005; Sofroniew and Vinters, 2010), and during the development of white matter, the loss or dysfunction of astrocytes leads to demyelination (Lutz et al., 2009). Astrocytes are also involved in transporting vital nutrients into the brain. The brain vasculature is almost entirely surrounded by astrocytic processes. These astrocytic end-feet are specific units that play a central role in maintaining the ionic and osmotic homeostasis of the CNS (Amiry-Moghaddam et al., 2003; Simard and Nedergaard, 2004). It has been postulated that astrocytic end-feet are an essential component of the neurovascular unit formed between brain capillary endothelial cells and pericytes (Abbott et al., 2006; Price et al., 2018), and that astrocytes can uptake nutrients directly from endothelial cells and distribute them into the CNS parenchyma.

Brain iron uptake is closely regulated by the blood brain barrier and specific transport mechanisms are needed to import this nutrient into the CNS (Rouault, 2006). Brain capillary endothelial cells express high levels of the transferrin receptor 1 (**Tfr1**) (Kawabata et al., 1999). Hence, Tfr-mediated uptake of iron by capillary endothelial cells is probably the main mechanism by which iron is transported into the brain, while only a small amount of iron is incorporated by the choroid plexuses (Crowe and Morgan, 1992). However, how iron is mobilized from endothelial cells into the brain parenchyma is not completely understood. The divalent metal transporter 1 (**DMT1**) and the Tfr1 are intensely expressed in astrocyte end-feet contacting endothelial cells (Burdo et al., 2001; Wang et al., 2001), suggesting that astrocytes can hypothetically absorb transferrin (**Tf**) and non-Tf bound iron directly from these cells. Unlike neurons or oligodendrocytes, astrocytes do not have an elevated metabolic iron requirement. Astrocytes contain limited ferritin, a highly conserved multimeric protein essential for intracellular iron storage (Connor et al., 1994; Liddell et al., 2006). In the normal CNS a limited number of astrocytes in discrete brain regions contain iron stored in ferritin (Connor et al., 1994; Liddell et al., 2006). This observation supports the concept that astrocytes may be predominantly implicated in brain iron trafficking rather than iron storage.

Iron is required for normal oligodendrocyte maturation and proper myelin production (Beard et al., 2003; Badaracco et al., 2008, 2010; Rosato-Siri et al., 2010); the extraordinary metabolic needs of oligodendrocytes is attributed to them having the highest iron levels of any cell type in the brain (Reinert et al., 2019). However, how iron homeostasis in astrocytes affects oligodendrocyte iron metabolism and myelin synthesis is unknown. Since most cells incorporate and mobilize iron via the Tf cycle, we knocked-out DMT1 and the Tfr1 in astrocytes. Moreover, we disrupted astrocytic iron storage by deleting the ferritin heavy

subunit (**Fth**) in Glast1-positive cells. These proteins were deleted in astrocytes throughout postnatal myelination as well as in the mature mouse brain. We found that Fth expression in astrocytes is essential for oligodendrocyte iron accumulation and myelination during early development. Furthermore, our data indicate that Fth iron storage in astrocytes is also relevant for an effective remyelination of the mouse brain. Collectively, these studies defined the participation of several proteins in astrocyte iron homeostasis as well as the role of astrocytes in brain iron metabolism.

MATERIALS AND METHODS

Transgenic mice

Procedures were approved by UB's Animal Care and Use Committee and performed following the National Institute of Health (NIH) guidelines. Floxed mouse lines were obtained from the Jackson Laboratory, including the divalent metal transporter 1 (**DMT1**) (Jackson Mice, # 017789), the transferrin receptor 1 (**Tfr1**) (Jackson Mice, # 028177), the ferritin heavy subunit (**Fth**) (Jackson Mice, # 018063) and the *Cre* reporter mouse line (Ai9(RCL-tdT) (Jackson Mice, # 007909). Experimental mice were created in our laboratory by crossing the homozygous floxed animals with hemizygous Glast1-*Cre*ER^{T2} transgenic mice (Jackson Mice, # 012586). Mice of either sex were used in all the experiments presented in this work.

Mice treatment

To knock-out the corresponding genes in Glast1-positive astrocytes, P2 Glast1-DMT1^{KO} (DMT1$^{f/f}$, Glast1-*Cre*$^{Cre/-}$), Glast1-Tfr^{KO} (Tfr$^{f/f}$, Glast1-*Cre*$^{Cre/-}$), Glast1-Fth^{KO} (Fth$^{f/f}$, Glast1-*Cre*$^{Cre/-}$) and control (*Cre*-negative) littermates (DMT1$^{f/f}$, Tfr$^{f/f}$ or Fth$^{f/f}$, Glast1-*Cre*$^{-/-}$) were intraperitoneally injected once a day for 5 consecutive days with 25 mg/kg tamoxifen (Sigma-Aldrich); brain tissues were collected at P15, P30 and P60. Furthermore, P60 Glast1-DMT1^{KO}, -Tfr^{KO}, -Fth^{KO} and control (*Cre*-negative) littermates were intraperitoneally injected with 100mg/kg of tamoxifen once a day for 5 consecutive days and brains were collected at P90. For remyelination studies, P60 Glast1-Fth^{KO} (Fth$^{f/f}$, Glast1-*Cre*$^{Cre/-}$) and control (*Cre*-negative) littermates were fed with 0.2% cuprizone in the pellet chow (Teklad-Envigo) for 7 weeks followed by a normal diet. Glast1-Fth^{KO} and control (*Cre*-negative) animals were injected with 100mg/kg of tamoxifen every other day for 2 weeks (total of 7 injections) starting after 5 weeks of cuprizone treatment.

Western blot

Western blots were performed as described in Santiago-González et al. (2017). Proteins (20μg/line) were separated using NuPAGE® Novex® 4–12% Bis-Tris Protein Gels (Life Technologies). Electroblotted PDVF membranes were blocked with 5% non-fat milk, 0.1% tween-20 in PBS overnight at 4°C. The same blocking solution was used to dilute the primary antibodies and membranes were incubated overnight at 4°C with agitation. Membranes were then scanned with a C-Digit Bot Scanner (LI-COR) and protein bands were detected by chemiluminescence using the Amersham ECL kit (GE Healthcare) with horseradish peroxidase-conjugated secondary antibodies (GE Healthcare). Protein bands were quantified using the Image Studio™ Software (LI-COR). Primary antibodies: CNP

(mouse; 1:1000; Neo-Markes), MBP (mouse; 1:1000; Biolegend) and p84 (mouse; 1:10,000; Genetex).

RT-PCR

RNA was isolated using Trizol reagent (Life Technologies). RNA purity and concentration were estimated by measuring the ratio of absorbance at 260/280nm. PCR primers were designed based on published sequences. cDNA was prepared from 1μg of total RNA using the PrimeScript 1st strand cDNA Synthesis Kit (Takara) and 2.5μM of oligo(dT). The mRNA samples were denaturized at 65°C for 5min and reverse transcription was performed at 42°C for 60min and was stopped by heating the samples at 95°C for 5min. The cDNA was amplified using specific primers and the PCR Platinum Super mix (Life Technologies). The PCR products were detected on a SYBR Safe stained agarose gel and the bands digitized using a Gel Doc™ EZ System (Bio-Rad).

Immunohistochemistry

Animals were anesthetized with avertin and perfused with 4% of paraformaldehyde in PBS via the left ventricle. Brains were then post-fixed overnight in the same fixative solution at 4°C. Free-floating vibratome sections (50μm thick) were incubated in a blocking solution (2% normal goat serum and 1% Triton X-100 in PBS) for 2hs at room temperature and then incubated with the primary antibody overnight at 4°C. Sections were then incubated with secondary antibodies (Cy3 or Cy5; 1:400; Jackson) for 2hs at room temperature and by the nuclear dye DAPI (Thermo Fisher Scientific). Finally, brain coronal slices were mounted on to Superfrost Plus Slides (Thermo Fisher Scientific) with Aquamount (Thermo Fisher Scientific). Antibodies: caspase-3 (mouse; 1:200; Cell Signaling), CC1 (mouse; 1:300; Calbiochem); CD31 (mouse; 1:200; Abcam); GFAP (rabbit, 1:1000; Dako), Ki67 (rabbit; 1:250; Abcam), Ki67 (mouse; 1:250; BD Biosciences), MBP (mouse; 1:400; Covance); NeuN (rabbit; 1:100; Millipore), Olig2 (mouse and rabbit; 1:500; Millipore), PLP (rat; 1:200; AA3-PLP/ DM20), s100β (rabbit, 1:800; Thermo Scientific) and 8-OHdG (mouse; 1:2000; StressMarq Biosciences). The staining intensity and the number of positive cells was assessed in the central area of the corpus callosum, between the midline and below the apex of the cingulum ($0.6mm^2$), in the somatosensory cortex ($0.6mm^2$) and in the dorsal/caudal striatum, immediately underneath the corpus callosum ($0.6mm^2$) (Franklin and Paxinos, 2008; Figure 24). Twenty slices per brain (50μm each) were photographed with an Olympus Spinning Disc Confocal Inverted Microscope (IX83) equipped with a CCD camera (Hamamatsu ORCA-R2). Three pictures (10X) per brain hemisphere were selected and quantification was performed using MetaMorph software (Molecular Devices). The integrated fluorescence intensity was calculated as the product of the area and mean pixel intensity. For all experiments involving quantification of positive cells and fluorescent intensity in tissue sections, the data represent pooled results from at least 4 brains per experimental group.

Electron microscopy

Mice were perfused with 3% paraformaldehyde and 1% glutaraldehyde via the left ventricle. The corpus callosum at the anterior-dorsal level of the hippocampus was dissected and embedded in resin. Thin sections were stained with uranyl acetate and lead citrate and

photographed with a FEI Tecnai F20 Transmission Electron Microscope (Cheli et al., 2016). The *g*-ratio and the percentage of myelinated axons was determined using MetaMorph software (Molecular Devices). The *g*-ratio was determined in at least 200 fibers per animal and the percentage of myelinated axons was calculated from 40 randomly selected fields per sample (>2000 axons).

Iron staining

Enhanced Perls histochemistry was performed as described previously in Cheli et al. (2018). Briefly, 20μm brain coronal sections were incubated with 1% H_2O_2 in methanol for 15min and then with 2% potassium ferrocyanide (pH 1.0) overnight (Iron Stain Kit, Sigma-Aldrich). The reaction was enhanced for 30min with 0.025% 3,3'-diaminobenzidine-4Hl, 0.05% H_2O_2 and 0.005% $CoCl_2$ in 0.1M PB. Sections were then dehydrated and mounted with Permount. Twelve slices per brain were used and the number of positive oligodendrocytes and the integrated staining intensity per cell was measured by MetaMorph software (Molecular Devices).

Black-gold staining

Black Gold II staining was performed as described in Cheli et al. (2016). Paraformaldehyde-fixed brain sections of 50μm were mounted onto Superfrost Plus slide (Fisher). Coronal brain slices were initially air dried and then rehydrated and transferred to a lukewarm 0.3% Black Gold II solution (Millipore). After 10min, the slides were rinsed with a 1% sodium thiosulfate solution at 60°C, dehydrated and mounted with Permount. Twenty slices per brain (50μm each) were used and the integrated staining intensity in the corpus callosum and cortex was assessed by MetaMorph software (Molecular Devices).

Statistical analysis

The Kolmogorov-Smirnov test was used to verify the normal distribution of all data sets. Single between-group comparisons were made by the unpaired t-test (Student's t-test), using a confidence interval of 95%. Multiple comparisons were investigated by one-way ANOVA followed by Bonferroni's multiple comparison test. The *g*-ratio distribution analysis was done by simple linear regression with a confidence interval of 95%. GraphPad Prism (GraphPad Software) was used to perform all the statistical tests. A value of $p<0.05$ for two-tailed test was the criterion for significant differences between experimental groups. For all the experiments data represent pooled results from at least 4 brains per experimental group.

RESULTS

Recombination analysis in the Glast1-CreER mouse line

Conditional KO mice for DMT1, Tfr1 and Fth were created by cross breeding the corresponding *floxed* lines (see Transgenic Mice for stock numbers) with the Glast1-*Cre*ER^{T2} mouse (Agarwal et al., 2017; Tran et al., 2018). The Glast1-*Cre*ER^{T2} transgenic mouse express a tamoxifen-inducible *Cre* recombinase under the mouse Glast1 promoter that restricts *Cre* expression to astrocytes (Tran et al., 2018). KO mice and control (*Cre*-negative) littermates were injected with tamoxifen during 5 consecutive days starting at P2

and brains were collected at P15, P30 and P60 for analysis (Figure 1A). Initially, total RNA was isolated form the cortex of P15 animals to evaluate *Cre* recombination efficiency by RT-PCR (Figure 1B). The presence of the expected truncated mRNA for DMT1, Tfr1 and Fth indicates a high *Cre* recombination efficacy in our conditional KO models (Figure 1B).

To determine the cell specificity of *Cre*-mediated DNA recombination, the Glast1-*Cre*ER^{T2} mouse was crossed with the *Cre* reporter line Ai9(RCL-tdT). The *Cre* reporter fluorescent protein tdTomato was combined with the oligodendrocyte lineage marker Olig2 and with the neuronal nuclear protein NeuN, and double-positive cells were analyzed in several brain areas (Figure 1D, F, E and H). With the sole exemption of the cortex, in which less than 1% of the Olig2 cells were positive for tdTomato, double-positive cells for Olig2/tdTomato or NeuN/tdTomato were not detected in any other brain area (Figure 1D, F, E and H). All the cortical and callosal tdTomato-positive cells showed the classic astrocyte morphology and more than 60% of these cells were positive for GFAP (Figure 1C and E). Furthermore, the vast majority of tdTomatao-positive astrocytes were in close contact with blood vessels (CD31-positive endothelial cells) (Figure 1G and H). Similar experiments were conducted in adult animals in which tamoxifen was administrated at P60 and brains were analyzed at P90. In these mice, tdTomato-positive astrocytes were found in great density across the CNS and ~50% of tdTomato-expressing cells in the cortex, corpus callosum and striatum were positive for GFAP (Figure 1I and K). Importantly, none of the tdTomato-expressing cells were positive for Olig2 or NeuN at P90 (Figure 1J and K).

Next, we made a series of immunohistochemistry experiments to analyze whether DMT1, Tfr1 and Fth ablation affects astrocyte development and/or proliferation. To test for astrocytes density, we did immunostainings against GFAP and s100β in the somatosensory cortex and corpus callosum (Figure 2). No significant changes in the numbers GFAP- or s100β-positive astrocytes were observed in conditional KO mice at P30 (Figure 2A, B, D and E). Furthermore, the morphological features and the anatomical distribution of these cells were found to be similar to controls (Figure 2A, B, D and E). Additionally, we quantified the proliferation of GFAP- and s100β-positive astrocytes by co-immunostaining these cells with Ki67, a protein present in mitotic cells. As shown in Figure 2C and F, the deletion of DMT1, Tfr1 or Fth did not affect astrocyte proliferation.

The importance of astrocyte iron metabolism in oligodendrocyte development

To examine how the activity of DMT1 in astrocytes affects the development of oligodendrocytes and the myelination of the CNS, **controls** (DMT1$^{f/f}$, Glast1-*Cre*$^{-/-}$) and **DMT1^{KO}** (DMT1$^{f/f}$, Glast1-*Cre*$^{Cre/-}$) offspring were treated with tamoxifen as described in Figure 1A. Initially, we performed immunohistochemistry for myelin proteins in several brain areas. We found less MBP and PLP immunofluorescent in the cortex, corpus callosum and striatum of DMT1^{KO} animals only at P15 (Figure 3A–D). Proteins were isolated from the corpus callosum of controls and DMT1^{KO} mice to evaluate myelin proteins by western blot (Figure 3E). In agreement with the immunohistochemistry data, DMT1^{KO} mice showed a decrease in MBP and CNP expression at P15, and a reduction in MBP levels at P30 (Figure 3E). Additionally, the total number of oligodendrocytes (Olig2-positive cells) and the density of mature myelinating oligodendrocytes (CC1-positive cells) were determined

in the cortex as well as in the central corpus callosum of controls and DMT1^{KO} mice (Figure 4). No statistical differences in the amount of Olig2-positive cells were found (Figure 4A and B), however, we detected a small reduction in the density of CC1-positive oligodendrocytes in cortical and callosal areas of DMT1^{KO} brains at P15 (Figure 4C and D), which lower the ratio of Olig2/CC1 double-positive cells (Figure 4E and F). Immunohistochemical experiments were also conducted in Glast1-Tfr^{KO} mice to analyze myelin protein synthesis and oligodendrocytes numbers. Compared to controls (Tfr$^{f/f}$, Glast1-*Cre*$^{-/-}$), Tfr^{KO} (Tfr$^{f/f}$, Glast1-*Cre*$^{Cre/-}$) mice displayed a small reduction in MBP and PLP expression specifically in the cortex and striatum at P15 (Figure 5A–D). Similarly, the expression of MBP and CNP by western blot was found to be only slightly reduced in the corpus callosum of Tfr^{KO} animals at P30 (Figure 5E). Furthermore, Tfr^{KO} brains exhibited normal numbers of Olig2- and CC1-positive cells in all brain areas and at all time-points (**data not shown**).

In contrast to the above-described results, Fth^{KO} animals presented a severe postnatal hypomyelination. Compared to **controls** (Fth$^{f/f}$, Glast1-*Cre*$^{-/-}$), **Fth^{KO}** (Fth$^{f/f}$, Glast1-*Cre*$^{Cre/-}$) brains displayed a significant decrease in MBP and PLP immunostaining in all brain areas (Figure 6A–D) and notably, the magnitude of these reductions was similar at all time-points (Figure 6A–D). Electron microscopy experiments were conducted in the corpus callosum to evaluate the myelin thickness and the proportion of myelinated axons. As shown in Figure 6E and F, the *g*-ratio of myelinated axons was drastically increased in Fth^{KO} mice. Axons of all sizes were affected, and these animals presented an important reduction in the percentage of myelinated axons and an increase in the average diameter of myelinated axons (Figure 6G). Additionally, total proteins were isolated from the corpus callosum of controls and Fth^{KO} brains to evaluate the expression of myelin proteins by western blot (Figure 6H). In agreement with the results described above, the expression levels of MBP and CNP were reduced in Fth^{KO} brains at P15, P30 and P60 (Figure 6H). We subsequently examined oligodendrocyte numbers in the cortex and central corpus callosum of controls and Fth^{KO} mice. No significant differences in the number of Olig2-positive cells were detected (Figure 7A and B), however, the density of mature CC1-positive oligodendrocytes in Fth^{KO} animals was lower than controls in all brain regions (Figure 7C and D). These changes lead to a marked reduction in the proportion of Olig2/CC1 double-positive cells (Figure 7E and F). Additionally, we analyzed apoptotic cell death in the somatosensory cortex and corpus callosum of Fth^{KO} mice by using a specific antibody against the activated form of Caspase-3 (Figure 7G). At P15, the quantity of apoptotic oligodendrocytes (Olig2/Casp-3 double-positive cells) was found to be equal to that of controls (Figure 7G).

We also conducted experiments in adult Glast1-KO mice to study how the ablation of DMT1, Tfr1 and Fth in astrocytes affects mature myelinating oligodendrocytes. For this set of experiments, controls and conditional KO animals were treated with tamoxifen at P60 and brain samples were collected for analysis at P90. The ablation of DMT1 or Tfr1 in astrocytes at P60 did not affect the expression of MBP and PLP in P90 brains (Figure 8A–E). P90 DMT1^{KO} and Tfr^{KO} mice also showed normal numbers of Olig2- and CC1-positive oligodendrocytes (Figure 8F). However, the synthesis of MBP and PLP in the cortex and corpus callosum of P90 Fth^{KO} mice was significantly reduced compare to controls (Figure

8A–D). This decline in the expression of myelin proteins was also detected by western blot (Figure 8E) and was correlated with similar reductions in the number of myelinating CC1-positive cells (Figure 8F).

Iron metabolism and oxidative stress in the brain of Glast1-KO mice

To measure intracellular iron quantities in oligodendrocytes, P30 conditional KO brains were stained for iron by the enhanced Perls histochemistry technique (Figure 9). The density of iron-positive oligodendrocytes as well as the staining intensity per cell was analyzed in the cortex and in the lateral section of the corpus callosum. $DMT1^{KO}$ and Tfr^{KO} mice displayed normal numbers of iron-positive oligodendrocytes and control levels of cell iron staining intensity (Figure 9A–D). In contrast, the cortex and the lateral section of the corpus callosum of Fth^{KO} animals showed a clear reduction in the number and staining intensity of iron-positive cells (Figure 9A–D). The iron staining intensity in cortical neurons and in brain areas such as the globus pallidus and the substantia nigra was also evaluated and found to be normal in all three conditional KO lines (**data not shown**).

We then determined whether the ablation of DMT1, Tfr1 and Fth in astrocytes affects neuronal numbers and/or induce brain oxidative stress. For this set of experiments, we used brain tissue slices from conditional KO and control animals collected at P60. Glast1-$DMT1^{KO}$, Tfr^{KO} and Fth^{KO} brains displayed control levels of NeuN-positive cells in the somatosensory cortex (Figure 10A and B. However, the cortical thickness of all three conditional KO mice was significantly reduced compare to controls (Figure 10A and B. The expression of the neurofilament L was also evaluated and found only to be reduced in Fth^{KO} brains (Figure 10B). Next, we immunolabeled somatosensory cortex sections of control and conditional KO animals to examine oxidative DNA and RNA damage in oligodendrocytes, astrocytes and neurons (Figure 10C–F. 8-hydroxyguanine (8-OHdG) is an oxidative derivative of guanosine and is a very sensitive marker of DNA and RNA oxidation (Kasai and Nishimura, 1983). An increase in 8-OHdG levels was detected in all brain areas of Fth^{KO} mice (Figure 10C and D. 8-OHdG immunosignal was primarily located in Fth^{KO} oligodendrocytes and neurons (Figure 10E and F, but a small increase in 8-OHdG immunostaining was also observed in cortical Fth^{KO} GFAP-positive cells (Figure 10E and F. In contrast, astrocytes and oligodendrocytes located in the cortex and striatum of Tfr^{KO} brains showed a significant reduction in 8-OHdG fluorescent intensity (Figure 10C–F). Furthermore, we analyzed apoptotic cell death in the somatosensory cortex of the three conditional KO mice (Figure 10G). At P60, the number of apoptotic oligodendrocytes, neurons and astrocytes in conditional KO brains were found to be equivalent to that of controls (Figure 10G).

Iron equilibrium in astrocyte during demyelination and remyelination

To define how the ablation of Fth in astrocytes affects the remyelination of the adult brain, we used the cuprizone model of demyelination and remyelination. P60 **controls** ($Fth^{f/f}$, Glast1-$Cre^{-/-}$) and **Fth^{KO}** ($Fth^{f/f}$, Glast1-$Cre^{Cre/-}$) mice were fed with cuprizone for 7 weeks to induce demyelination and were injected with tamoxifen every other day during the last two weeks of the cuprizone diet to delete the Fth gene specifically in astrocytes. Brains were then collected after 7 weeks of cuprizone treatment (**7W CPZ**) and at 2 or 4 weeks

of recovery in normal diet (**2W or 4W Rec**). Additionally, brain tissue from mice that were not treated with cuprizone or tamoxifen were used as untreated controls (**Untreated**). The remyelination of the Fth^{KO} brain was initially evaluated using the Black Gold staining technique for myelin. Cuprizone treatment induced a severe demyelination in the brain of both controls and Fth^{KO} mice (Figure 11A and B). Importantly, at this time-point we found a further decrease of myelin staining in the corpus callosum of Fth^{KO} mice (Figure11A and B). A significant remyelination was observed in the cortex, corpus callosum and striatum of both genotypes during the remyelination phase of the cuprizone model (Figure 11A and B), although, suggesting a deficit in remyelination, Fth^{KO} mice showed significantly less myelin staining than controls after 2 and 4 weeks of recovery (Figure 11A and B). These reductions were also found in western blot experiments for myelin proteins (Figure 11C and D). Remyelination was also evaluated by immunohistochemistry for myelin proteins (Figure 12A and B). The cortex of Fth^{KO} animals presented a significant reduction in the amount of PLP and MBP (Figure 12A and B); these changes were detected at the end of the cuprizone treatment as well as during the recovery phase (Figure 12A and B). We found no differences in the number of Olig2-positive cells among genotypes in any of the experimental conditions (Figure 12C). However, we noticed a decline in the number of CC1-positive cells after 2 and 4 weeks of recovery in Fth deficient mice (Figure 12C). These reductions significantly affected the percentage of Olig2-positive cells expressing CC1 (Figure 12D). Additionally, seven weeks of cuprizone treatment induces a severe astrogliosis in both controls and Fth^{KO} animals (Figure 12A and E). Reactive GFAP-positive astrocytes reached maximum levels at the end of the cuprizone treatment and began to decline at 2 weeks of recovery (Figure 12A and E). However, no changes in the density of GFAP- or GFAP/Ki67-positive cells were noticed among genotypes (Figure 12A and E).

DISCUSSION

Iron incorporation in astrocytes and oligodendrocyte maturation

We have found that the specific deletion of DMT1 or Tfr1 in astrocytes during the first postnatal week do not significantly affect brain myelination and/or oligodendrocyte development. Although we found minor reductions in the expression of myelin proteins at P15, these changes were transient and disappeared later in development. At P30 and P60, $DMT1^{KO}$ and Tfr^{KO} brains showed no significant changes in the production of myelin proteins and displayed normal numbers of mature myelinating oligodendrocytes. Furthermore, the density of iron-positive cells in $DMT1^{KO}$ and Tfr^{KO} mice was found to be identical to controls. Similar results were found in adult (P90) mice in which DMT1 and Tfr1 were ablated in astrocytes at P60. In these animals, the number of mature oligodendrocytes as well as the synthesis of myelin proteins was normal.

These results suggest that the Tf cycle—in which DMT1 and the Tfr1 are essential components—plays a secondary role in astrocyte iron metabolism, and that the expression of these proteins in astrocytes is not crucial for brain iron homeostasis and/or oligodendrocyte iron incorporation. However, DMT1 and Tfr1 are strongly expressed in the astrocyte end-feet that contact capillary endothelial cells (Wang et al., 2001; Jeong and David, 2003; Erikson and Aschner 2006; Pelizzoni et al., 2013), which suggests that astrocytes are

qualified to uptake Tf and non-Tf iron bound at the blood brain barrier. Zip14 is an alternative iron transporter which is also localized to the astrocytic plasma membrane and its overexpression increases the uptake of non-Tf iron bound to astrocytes (Qian et al., 2000; Liuzzi et al., 2006; Lane et al., 2010; Aydemir and Cousins, 2018). Astrocytes release nucleotides and citrate which could act as mediators of iron release from Tf (Sonnewald et al., 1991; Montana et al., 2006). Thus, astrocytes may upregulate Zip14 to compensate the absence of DMT1 and/or Tfr1 early during brain development.

Blocking the expression of DMT1 or Tfr1 in astrocytes did not affect the density of cortical neurons or the expression of neurofilaments, but significantly reduced cortical thickness. These changes suggest that brain maturation is not completely normal in these animals. Diminished cortical thickness is usually associated with reductions in the number of neurons and/or declines in neuronal conectivity and both of these factors are typically associated with deficits in neuronal development or survival. However, both the number of NeuN-positive cells and the amount of apoptotic neurons were normal in $DMT1^{KO}$ and Tfr^{KO} brains. Futhermore, no signs of neuronal oxidative stress were found in these animals—suprisingly, Tfr^{KO} astrocytes and oligodendrocytes displayed a reduction in the fluorescent intensity of 8-OHdG. Additionally, the iron content of cortical neurons in $DMT1^{KO}$ and Tfr^{KO} brains was similar to controls. Still, it is posible that DMT1 and Tfr1 deletion in astrocytes induces oxidative stress and/or iron deficiency in neurons very early during brain maturation. Thus, more experiments are needed to define this potential scenario.

Astrocytic ferritin is crucial for postnatal myelination

Ferritin, the primary intracellular iron-storage protein, is composed of heavy (Fth) and light (Ftl) chains and capable of binding more than 4,500 atoms of iron which can be mobilized for metabolic purposes through lysosomal degradation (De Domenico et al., 2006; Cohen et al., 2010). Ferritin-positive astrocytes are observed in several brain regions and the expression of this protein in astrocytes increases with age (Dickinson and Connor, 1995; Han et al., 2002). Astrocytes *in vitro* contain low amounts of ferritin (Regan et al., 2002; Hoepken et al., 2004), however, elevated iron availability or hypoxic conditions strongly increase ferritin expression in cultured astrocytes (Regan et al., 2002; Hoepken et al., 2004; Irace et al., 2005). Our results suggest that Fth synthesis in astrocytes plays an important role in early oligodendrocyte iron homeostasis and development. Knocking-out Fth in astrocytes significantly reduced myelin production throughout the first two postnatal months; Fth^{KO} animals displayed a substantial decrease in the percentage of myelinated axons and a rise in the average diameter of myelinated axons, suggesting a delay in the myelination process. Fth^{KO} brains showed a decline in the number of mature (CC1-positive) oligodendrocytes and in the percentage of Olig2/CC1 double-positive cells, but no significant changes in the density of total oligodendrocytes or in the number of apoptotic cells were found. Thus, the reduction in myelinating oligodendrocytes detected in Fth^{KO} mice during development is not a consequence of increased cell death and/or reduced oligodendrocyte generation, but likely the outcome of delayed oligodendrocyte maturation. The hypomyelination of young Fth^{KO} animals was also present in adult P90 mice, suggesting that Fth synthesis in astrocytes is also relevant for oligodendrocyte function in the adult brain.

Importantly, cortical and callosal oligodendrocytes of the Fth^{KO} CNS showed clear signs of iron deficiency. It has been suggested that immature oligodendrocytes uptake iron by incorporating ferritin rather than iron associated to Tf (Rouault, 2013). Oligodendrocytes bind ferritin and that ferritin binds to white matter brain areas (Todorich et al., 2008). In culture, ferritin released by iron-loaded microglial cells stimulates oligodendrocyte development (Zhang et al., 2006). Tim-2 (T-cell immunoglobulin and mucin domain-containing protein-2) was proposed to be the exclusive receptor by which oligodendroglial cells uptake ferritin (Todorich et al., 2008). It is possible that astrocytes and microglial cells secrete iron-loaded ferritin to distribute and share iron with other cell types of the CNS. Thus, during postnatal development a significant amount of iron could be delivered to immature oligodendrocytes via astrocytic ferritin.

Fth^{KO} animals displayed normal numbers of astrocytes and neurons and no signs of increased apoptotic cell death during development. However, these animals exhibited a reduction in the cortical thickness and in the expression of neurofilaments at P60. These changes were accompanied with signs of oxidative stress in oligodendrocytes, neurons and astrocytes. Oxidative stress is a potent driving force for myelin and neuronal injury, and oligodendrocytes can be easily damaged by oxidative stress, especially during the myelination process (Roth and Nuñez, 2016; Giacci et al., 2018). For this reason, oxidative stress is under physiological conditions limited by numerous anti-oxidant mechanisms, which are largely present in microglial cells and astrocytes (Lassman and Horssen, 2016). As a result of its ability to sequester iron efficiently, Fth is considered an antioxidant protein (Balla et al., 2007). For instance, Fth secreted by myelinating oligodendrocytes protects axons against iron-mediated injury in the mouse brain (Mukherjee et al., 2020). Similarly, Fth secreted by astrocytes can potentially provide an antioxidant shield to neurons and oligodendrocytes during development. The absence of Fth in astrocytes might also induce high intracellular iron concentrations and mitochondrial damage. Furthermore, brain oxidative stress could be amplified by the liberation of ferrous iron from Fth-deficient astrocytes, which can lead to the formation of highly reactive hydroxyl radicals (Papanikolaou and Pantopoulos, 2005). Thus, these mechanisms may jointly contribute to oligodendrocyte and neuronal oxidative stress, as well as myelin injury, in young and adult Fth^{KO} mice and be responsible, at least partially, for the hypomyelination observed in these animals.

Ferritin synthesis in astrocytes and the remyelination of the adult brain

Brain iron metabolism has been shown to be severely disturbed in demyelinating diseases. For instance, magnetic resonance imaging studies have shown iron accumulation in the brain of multiple sclerosis (MS) patients (Bakshi et al., 2002; Neema et al., 2009). Activated astrocytes and reactive microglia are the cell types in which this iron accumulation predominantly occurs (Rouault, 2013; Hametner et al., 2013). In the EAE model of MS, iron deposits were found in reactive microglia and astrocytes in both gray and white matter structures (Zamboni, 2006; Singh and Zamboni, 2009; Williams et al., 2011). In demyelinating lesions astrocytes up-regulate DMT1, Tfr1 and Zip14, which suggests that these cells can potentially uptake and safely recycle iron after myelin injury (Zarruk et al., 2015). In a mouse model of focal chemical demyelination, oligodendrocyte maturation and

remyelination were reduced when ferroportin, the only known iron exporter, was exclusively ablated in astrocytes (Schulz et al., 2012).

Our data indicate that Fth iron storage in astrocytes is crucial for an efficient remyelination of the adult brain. Throughout demyelination and remyelination, Fth^{KO} brains presented normal numbers of reactive and proliferating astrocytes. However, at the end of the cuprizone treatment and during the recovery phase we noticed a decline in the quantity of mature oligodendrocytes and in the expression of myelin proteins. Importantly, the total number of oligodendrocytes was normal, suggesting that the main problem of Fth^{KO} mice during remyelination is not oligodendrocyte proliferation or survival, but rather the maturation of the oligodendrocyte population. Astrocytic Fth can be the primary source of iron for newly generated oligodendrocytes in the demyelinated brain and Fth synthesis in astrocytes might be central to store and safely recycle iron from dead oligodendrocytes. More experiments are needed to define the role of astrocytic Fth in the remyelinating mouse brain. However, our data highlight the importance of astrocyte iron homeostasis in demyelinating diseases and suggest that iron storage in astrocytes can significantly impact the efficiency of the remyelination process.

Acknowledgements:

National Institute of Neurological Disorders and Stroke (award number: R01NS07804) and startup package from the Jacobs School of Medicine and Biomedical Sciences, University at Buffalo.

REFERENCES

Abbott NJ, Rönnbäck L, Hansson E (2006) Astrocyte-endothelial interactions at the blood-brain barrier. Nat Rev Neurosci 7: 41–53. [PubMed: 16371949]

Agarwal A, Wu PH, Hughes EG, Fukaya M, Tischfield MA, Langseth AJ, Wirtz D, Bergles DE (2017) Transient opening of the mitochondrial permeability transition pore induces microdomain calcium transients in astrocyte processes. Neuron 93: 587–605. [PubMed: 28132831]

Amiry-Moghaddam M, Otsuka T, Hurn PD, Traystman RJ, Haug MF, Froehner SC, Adams ME, Neely JD, Agre P, Ottersen OP, Bhardwaj A (2003) An alphasyntrophin-dependent pool of AQP4 in astroglial end-feet confers bidirectional water flow between blood and brain. Proc Natl Acad Sci USA 100: 2106–2111. [PubMed: 12578959]

Aydemir TB, Cousins RJ (2018) The multiple faces of the metal transporter Zip14 (SLC39A14). The Journal of nutrition 148: 174–184. [PubMed: 29490098]

Badaracco ME, Ortiz EH, Soto EF, Connor JR, Pasquini JM (2008) Effect of transferrin on hypomyelination induced by iron deficiency. J Neurosci Res 86: 2663–73. [PubMed: 18459135]

Badaracco ME, Siri MVR, Pasquini JM (2010) Oligodendrogenesis: The role of iron. Bio Factors, 36: 98–102.

Bakshi R, Benedict RH, Bermel RA, Caruthers SD, Puli SR, Tjoa CW, Fabiano AJ, Jacobs L (2002) T2 hypointensity in the deep gray matter of patients with multiple sclerosis, a quantitative magnetic resonance imaging study. Arch Neurol 59: 62–68. [PubMed: 11790232]

Balla J, Vercellotti GM, Jeney V, Yachie A, Varga Z, Jacob HS, Eaton JW, Balla G (2007) Heme, heme oxygenase, and ferritin: how the vascular endothelium survives (and dies) in an iron-rich environment. Antioxid Redox Signal 9: 2119–2137. [PubMed: 17767398]

Beard JL, Wiesinger JA, Connor JR (2003) Pre- and postweaning iron deficiency alters myelination in Sprague-Dawley rats. Dev Neurosci 25: 308–315. [PubMed: 14614257]

Burdo JR, Menzies SL, Simpson IA, Garrick LM, Garrick MD, Dolan KG, Haile DJ, Beard JL, Connor JR (2001) Distribution of divalent metal transporter 1 and metal transport protein 1 in the normal and Belgrade rat. J Neurosci Res 66:1198–1207. [PubMed: 11746453]

Cheli VT, Santiago Gonzalez DA, Marziali LN, Zamora NN, Guitart ME, Spreuer V, Pasquini JM, Paez PM (2018) The divalent metal transporter 1 (DMT1) is required for iron uptake and normal development of oligodendrocyte progenitor cells. J Neurosci 38: 9142–9159. [PubMed: 30190412]

Cheli VT, Santiago González DA, Namgyal Lama T, Spreuer V, Handley V, Murphy GG and Paez PM (2016) Conditional deletion of the L-type calcium channel Cav1.2 in oligodendrocyte progenitor cells affects postnatal myelination in mice. J Neurosci 36: 10853–10869. [PubMed: 27798140]

Christopherson KS, Ullian EM, Stokes CC, Mullowney CE, Hell JW, Agah A, Lawler J, Mosher DF, Bornstein P, Barres BA (2005) Thrombospondins are astrocyte-secreted proteins that promote CNS synaptogenesis. Cell 120: 421–33. [PubMed: 15707899]

Cohen LA, Gutierrez L, Weiss A, Leichtmann-Bardoogo Y, Zhang D, Crooks DR, Sougrat R, Morgenstern A, Galy B, Hentze MW, Lazaro FJ, Rouault TA, Meyron-Holtz EG (2010) Serum ferritin is derived primarily from macrophages through a nonclassical secretory pathway. Blood 116: 1574–1584. [PubMed: 20472835]

Connor JR, Boeshore KL, Benkovic SA, Menzies SL (1994) Isoforms of ferritin have a specific cellular distribution in the brain. J Neurosci Res 37: 461–465. [PubMed: 8021970]

Crowe A, Morgan EH (1992) Iron and transferrin uptake by brain and cerebrospinal fluid in the rat. Brain Res 592: 8–16. [PubMed: 1450923]

De Domenico I, Vaughn MB, Li L, Bagley D, Musci G, Ward DM, Kaplan J (2006) Ferroportin-mediated mobilization of ferritin iron precedes ferritin degradation by the proteasome. EMBO J 25: 5396–5404. [PubMed: 17082767]

Dickinson TK, Connor JR (1995) Cellular distribution of iron, transferrin, and ferritin in the hypotransferrinemic (Hp) mouse brain. J Comp Neurol 355: 67–80. [PubMed: 7636015]

Erikson KM, Aschner M (2006) Increased manganese uptake by primary astrocyte cultures with altered iron status is mediated primarily by divalent metal transporter. Neurotoxicology 27: 125–130. [PubMed: 16140386]

Franklin KBJ, Paxinos G (2008) The mouse brain in stereotaxic coordinates. 3. New York Academic Press.

Giacci MK, Bartlett CA, Smith NM, Iyer KS, Toomey LM, Jiang H, Guagliardo P, Kilburn MR, Fitzgerald M (2018) Oligodendroglia are particularly vulnerable to oxidative damage after neurotrauma *in vivo*. J Neurosci 38: 6491–6504. [PubMed: 29915135]

Hametner S, Wimmer I, Haider L, Pfeifenbring S, Brück W, Lassmann H (2013) Iron and neurodegeneration in the multiple sclerosis brain. Ann Neurol 74: 848-861. [PubMed: 23868451]

Han J, Day JR, Connor JR (2002) H and L ferritin subunit mRNA expression differs in brains of control and iron-deficient rats. J Nutr 132: 2769–2774. [PubMed: 12221243]

Hoepken HH, Korten T, Robinson SR, Dringen R (2004) Iron accumulation, iron-mediated toxicity and altered levels of ferritin and transferrin receptor in cultured astrocytes during incubation with ferric ammonium citrate. J Neurochem 88: 1194–1202. [PubMed: 15009675]

Irace C, Scorziello A, Maffettone C, Pignataro G, Matrone C, Adornetto A, Santamaria R, Annunziato L, Colonna A (2005) Divergent modulation of iron regulatory proteins and ferritin biosynthesis by hypoxia/reoxygenation in neurones and glial cells. J Neurochem 95: 1321–1331. [PubMed: 16135072]

Jeong SY, David S (2003) Glycosylphosphatidylinositol-anchored ceruloplasmin is required for iron efflux from cells in the central nervous system. J Biol Chem 278: 27144–27148. [PubMed: 12743117]

Kasai H, Nishimura S (1983) Hydroxylation of the C-8 position of deoxyguanosine by reducing agents in the presence of oxygen. Nucleic Acids Symp 12: 165–167.

Kawabata H, Yang R, Hirama T, Vuong PT, Kawano S, Gombart AF, Koeffler HP (1999) Molecular cloning of transferrin receptor 2. A new member of the transferrin receptor-like family. J Biol Chem 274: 20826–20832. [PubMed: 10409623]

Lane DJ, Robinson SR, Czerwinska H, Bishop GM, Lawen A (2010) Two routes of iron accumulation in astrocytes: ascorbate-dependent ferrous iron uptake via the divalent metal transporter (DMT1) plus an independent route for ferric iron. Biochem J 432:123–132. [PubMed: 20819077]

Lassmann H, van Horssen J (2016) Oxidative stress and its impact on neurons and glia in multiple sclerosis lesions. Biochim Biophys Acta 1862: 506–510. [PubMed: 26432481]

Liddell JR, Hoepken HH, Crack PJ, Robinson SR, Dringen R (2006) Glutathione peroxidase 1 and glutathione are required to protect mouse astrocytes from iron-mediated hydrogen peroxide toxicity. J Neurosci Res 84: 578–586. [PubMed: 16721761]

Liuzzi JP, Aydemir F, Nam H, Knutson MD, Cousins RJ (2006) Zip14 (Slc39a14) mediates non-transferrin-bound iron uptake into cells. Proc Natl Acad Sci U S A 103: 13612–13617. [PubMed: 16950869]

Lutz SE, Zhao Y, Gulinello M, Lee SC, Raine CS, Brosnan CF (2009) Deletion of astrocyte connexins 43 and 30 leads to a demyelinating phenotype and hippocampal CA1 vacuolation. J Neurosci 29: 7743–7752. [PubMed: 19535586]

Montana V, Malarkey EB, Verderio C, Matteoli M, Parpura V (2006) Vesicular transmitter release from astrocytes. Glia 54: 700–715. [PubMed: 17006898]

Mukherjee C, Kling T, Russo B, Miebach K, Kess E, Schifferer M, Pedro LD, Weikert U, Fard MK, Kannaiyan N, Rossner M, Aicher ML, Goebbels S, Nave KA, Krämer-Albers EM, Schneider A, Mikael Simons M (2020) Oligodendrocytes provide antioxidant defense function for neurons by secreting ferritin heavy chain. Cell Metab 32: 259–272. [PubMed: 32531201]

Neema M, Arora A, Healy BC, Guss ZD, Brass SD, Duan Y, Buckle GJ, Glanz BI, Stazzone L, Khoury SJ, Weiner HL, Guttmann CR, Bakshi R (2009) Deep gray matter involvement on brain MRI scans is associated with clinical progression in multiple sclerosis. J Neuroimaging 19: 3–8. [PubMed: 19192042]

Papanikolaou G, Pantopoulos K (2005) Iron metabolism and toxicity. Toxicol Appl Pharmacol 202: 199-211. [PubMed: 15629195]

Pelizzoni I, Zacchetti D, Campanella A, Grohovaz F, Codazzi F (2013) Iron uptake in quiescent and inflammation-activated astrocytes: a potentially neuroprotective control of iron burden. Biochim Biophys Acta 1832: 1326–1333. [PubMed: 23583428]

Price BR, Norris CM, Sompol P, Wilcock DM (2018) An emerging role of astrocytes in vascular contributions to cognitive impairment and dementia. J Neurochem 144: 644–650. [PubMed: 29222909]

Qian ZM, Liao QK, To Y, Ke Y, Tsoi YK, Wang GF, Ho KP (2000) Transferrin-bound and transferrin free iron uptake by cultured rat astrocytes. Cell Mol Biol 46: 541–548. [PubMed: 10872741]

Regan RF, Kumar N, Gao F, Guo Y (2002) Ferritin induction protects cortical astrocytes from heme-mediated oxidative injury. Neuroscience 113: 985–994. [PubMed: 12182902]

Reinert A, Morawski M, Seeger J, Arendt T, Reinert T (2019) Iron concentrations in neurons and glial cells with estimates on ferritin concentrations. BMC Neurosci 20: 25. [PubMed: 31142282]

Rosato-Siri MV, Badaracco ME, Ortiz EH, Belforte N, Clausi MG, Soto EF, Bernabeu R, Pasquini JM (2010) Oligodendrogenesis in iron-deficient rats: effect of apotransferrin. J Neurosci Res 8: 1695–1707.

Roth AD, Núñez MT (2016) Oligodendrocytes: functioning in a delicate balance between high metabolic requirements and oxidative damage. Adv Exp Med Biol 949: 167–181. [PubMed: 27714689]

Rouault TA (2006) The role of iron regulatory proteins in mammalian iron homeostasis and disease. Nat Chem Biol 2: 406–414. [PubMed: 16850017]

Rouault TA (2013) Iron metabolism in the CNS: implications for neurodegenerative diseases. Nat Rev Neurosci 14: 551–564. [PubMed: 23820773]

Santiago-González DA, Cheli VT, Zamora NN, Namgyal Lama T, Spreuer V, Murphy GG, Paez PM (2017) Conditional deletion of the L-type calcium channel Cav1.2 in NG2 positive cells delay remyelination in mice. J Neurosci 37: 10038–10051. [PubMed: 28899915]

Schulz K, Kroner A, David S (2012) Iron efflux from astrocytes plays a role in remyelination. J Neurosci 32: 4841-4847. [PubMed: 22492039]

Simard M, Nedergaard M (2004) The neurobiology of glia in the context of water and ion homeostasis. Neuroscience 129: 877–896. [PubMed: 15561405]

Singh AV, Zamboni P (2009) Anomalous venous blood flow and iron deposition in multiple sclerosis. J Cereb Blood Flow Metab 29: 1867–1878. [PubMed: 19724286]

Sofroniew MV, Vinter HV (2010) Astrocytes: biology and pathology. Acta Neuropathol 119: 7–35. [PubMed: 20012068]

Sonnewald U, Westergaard N, Krane J, Unsgård G, Petersen SB, Schousboe A (1991) First direct demonstration of preferential release of citrate from astrocytes using [13C] NMR spectroscopy of cultured neurons and astrocytes. Neurosci Lett 128: 235–239. [PubMed: 1945042]

Todorich B, Zhang X, Slagle-Webb B, Seaman WE, Connor JR (2008) Tim-2 is the receptor for H-ferritin on oligodendrocytes. J Neurochem 107: 1495–505. [PubMed: 19014383]

Tran CHT, Peringod G, Gordon GR (2018) Astrocytes integrate behavioral state and vascular signals during functional hyperemia. Neuron 100: 1133–1148. [PubMed: 30482689]

Wang XS, Ong WY, Connor JR (2001) A light and electron microscopic study of the iron transporter protein DMT1 in the monkey cerebral neocortex and hippocampus. J Neurocytol 30: 353–360. [PubMed: 11875282]

Williams R, Rohr AM, Wang WT, Choi IY, Lee P, Berman NEJ, Lynch SG, LeVine SM (2011) Iron deposition is independent of cellular inflammation in a cerebral model of multiple sclerosis. BMC Neuroscience 12: 59. [PubMed: 21699685]

Zamboni P (2006) The big idea: iron-dependent inflammation in venous disease and proposed parallels in multiple sclerosis. J R Soc Med 99: 589–593. [PubMed: 17082306]

Zarruk JG J Berard JL, Passos dos Santos R, Kroner A, Lee J, Arosio P, David S (2015) Expression of iron homeostasis proteins in the spinal cord in experimental autoimmune encephalomyelitis and their implications for iron accumulation. Neurobiol Dis 81: 93-107. [PubMed: 25724358]

Zhang X, Surguladze N, Slagle-Webb B, Cozzi A, Connor JR (2006) Cellular iron status influences the functional relationship between microglia and oligodendrocytes. Glia 54: 795–804. [PubMed: 16958088]

MAIN POINTS

- H-ferritin deletion in astrocytes induced hypomyelination and reduced oligodendrocyte iron incorporation and development.
- Blocking H-ferritin expression in astrocytes after demyelination impaired oligodendrocyte maturation and remyelination.

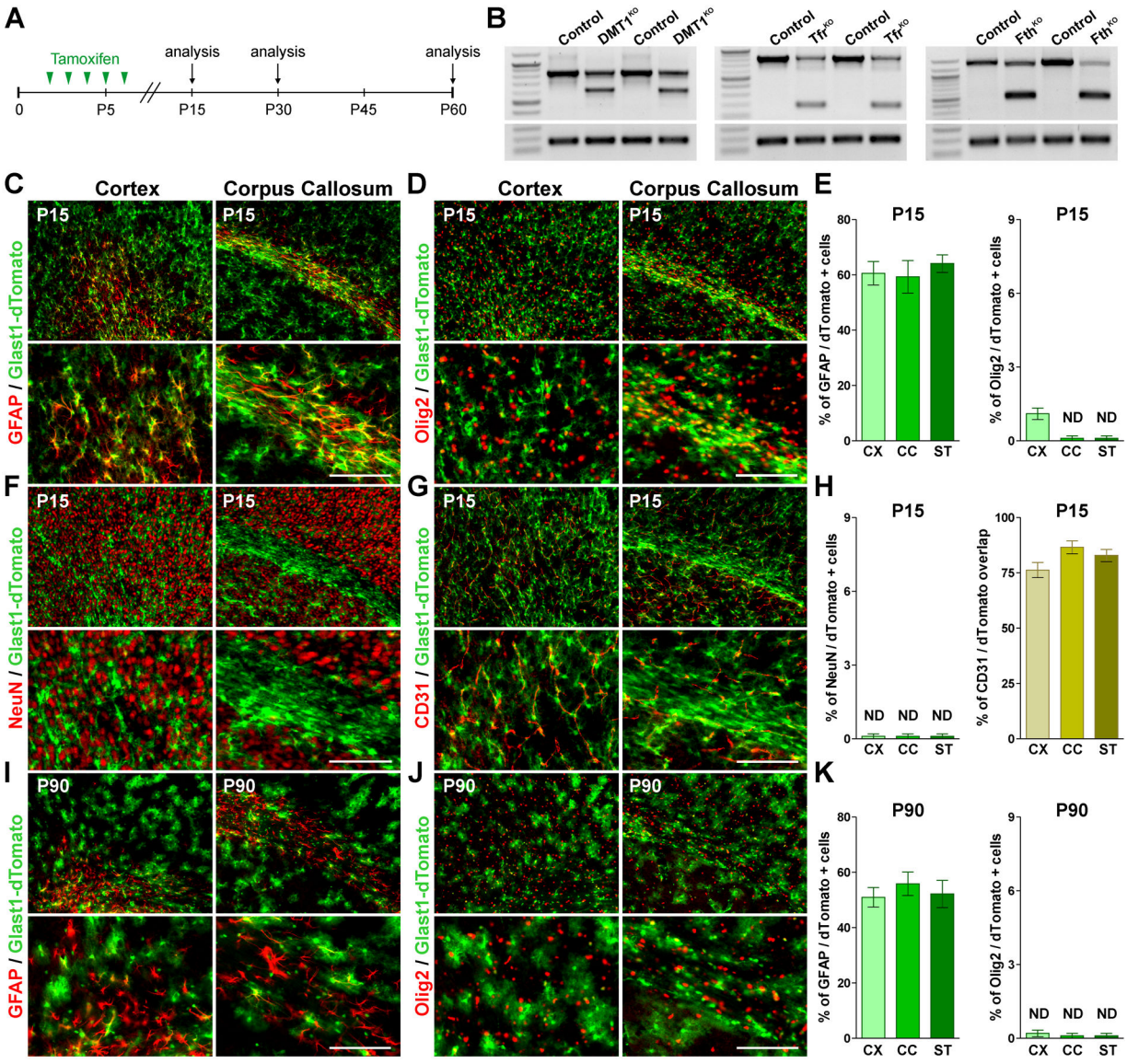

FIGURE 1: Recombination efficiency in the postnatal Glast1-dTomato mouse.

(**A**) P2 Glast1-KO lines and control (*Cre*-negative) littermates received 5 consecutive tamoxifen injections and brain tissue was collected at P15, P30 and P60. (**B**) Semi-quantitative RT-PCRs for DMT1, Tfr1 and Fth were performed at P15 with RNA isolated from the cortex of control and corresponding Glast1-KO mice. (**C, D, F and G**) GFAP, Olig2, NeuN and CD31 immunostaining in the brain of Glast1-dTomato mice at P15. Scale bar=90μm upper panel, 45μm lower panel. (**E and H**) Percentage of GFAP/, Olig2/ and NeuN/dTomato double-positive cells and overlap between CD31 and dTomato in the somatosensory cortex (**CX**), lateral corpus callosum (**CC**) and striatum (**ST**). (**I and J**) GFAP and Olig2 immunostaining in the brain of Glast1-dTomato mice at P90. Scale bar=90μm upper panel, 45μm lower panel. (**K**) Percentage of GFAP/dTomato and Olig2/ dTomato in the CX, CC and ST. Values are expressed as mean ± SEM.

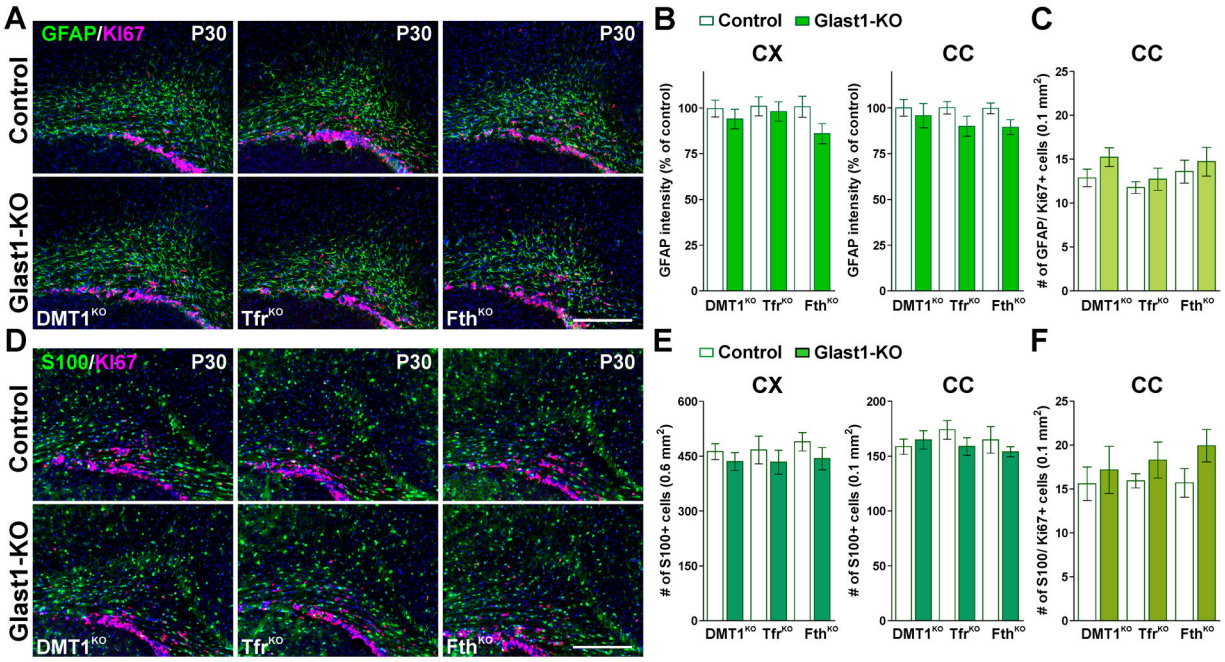

FIGURE 2: Astrocytes numbers in Glast1-KO animals.

(**A and D**) GFAP, s100β and Ki67 immunostaining in the brain of control and Glast1-KO mice at P30. Scale bar=90μm. (**B and E**) GFAP fluorescence intensity and total number of s100β-positive cells in the CX and CC. (**C and F**) Total number of GFAP/ and s100β/Ki67 double-positive cells in the CC at P30. Values are expressed as mean ± SEM.

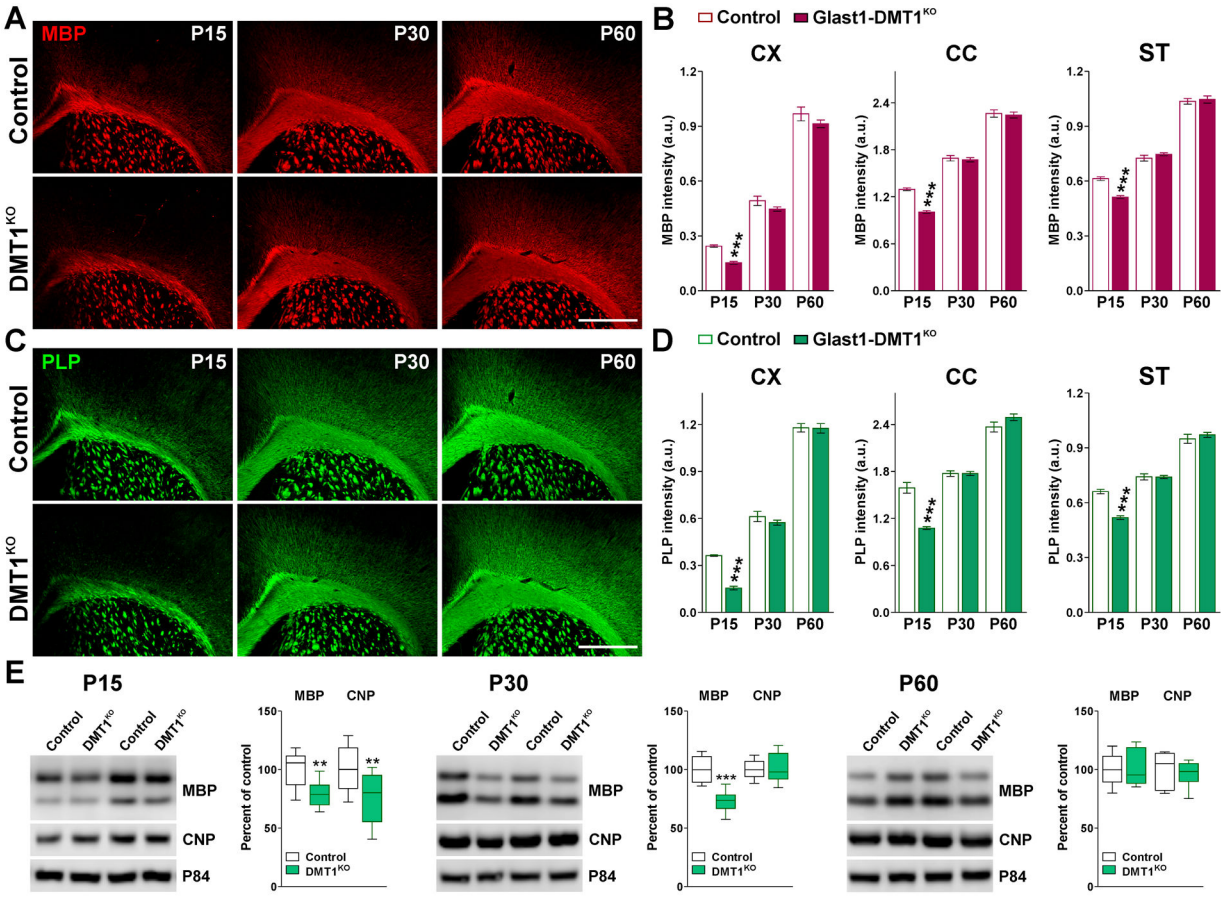

FIGURE 3: Myelin proteins in the postnatal Glast1-DMT1^{KO} mouse.

(**A and C**) MBP and PLP immunostaining in the brain of control and Glast1-DMT1^{KO} mice at P15, P30 and P60. Scale bar=180μm. (**B and D**) Integrated fluorescence intensity for MBP and PLP in the CX, CC and ST. Values are expressed as mean ± SEM. ***p<0.001 vs. respective controls. (**E**) Representative western blots for MBP and CNP in the CC of control and Glast1-DMT1^{KO} animals at P15, P30 and P60. P84 was used as the internal standard and box-and-whisker plots are showing means ± SD from 4 independent experiments. **p<0.01, ***p<0.001 vs. respective controls.

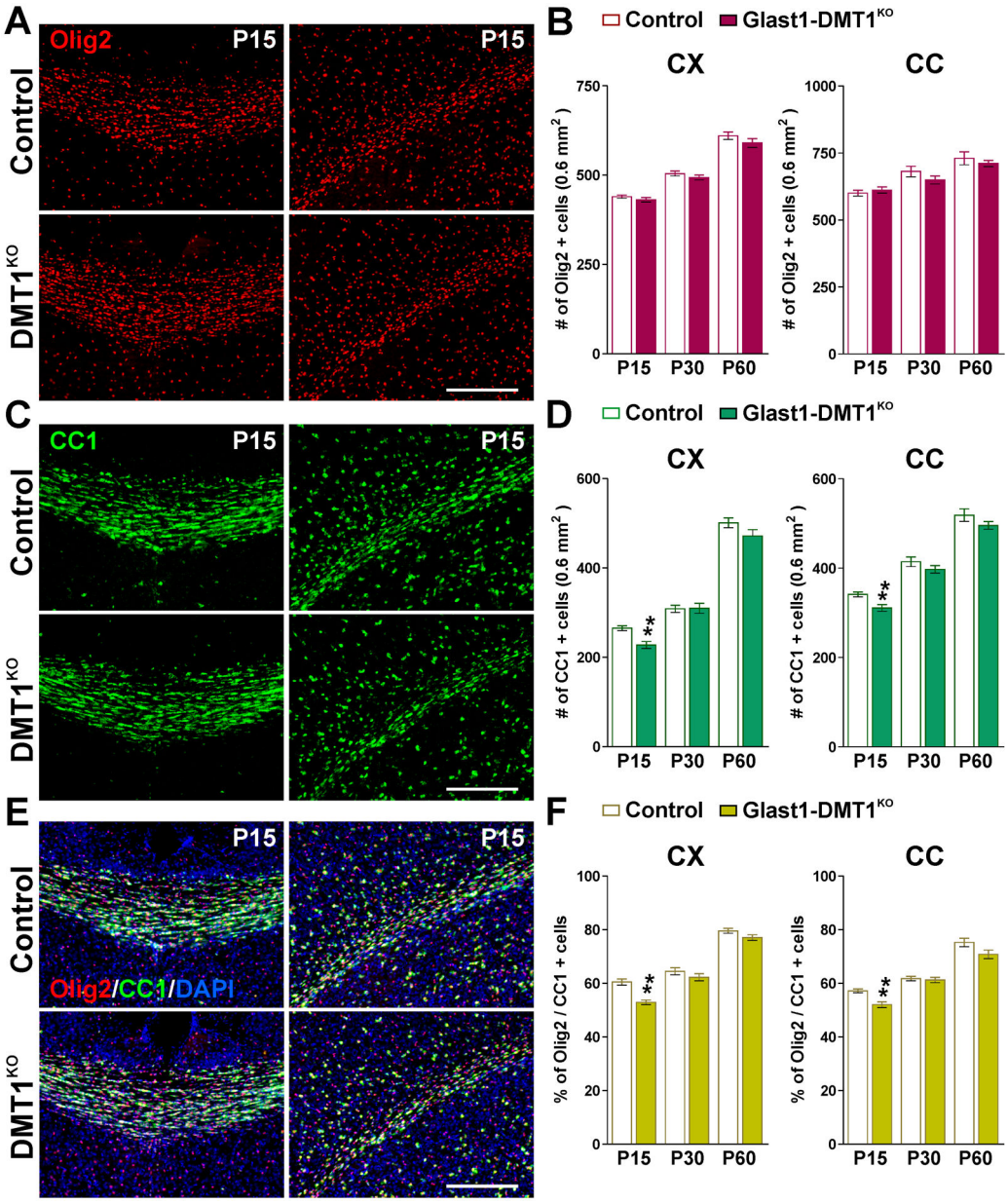

FIGURE 4: Oligodendrocyte numbers in Glast1-DMT1^{KO} brain during early development.

(**A, C and E**) Brain coronal sections from control and Glast1-DMT1^{KO} mice immunostained for Olig2 and CC1 at P15. Scale bar=90μm. (**B, D and F**) Total number of Olig2 and CC1-positive cells and percentage of Olig2/CC1 double-positive cells in the CX and CC at P15, P30 and P60. Values are expressed as mean ± SEM. *p<0.05, **p<0.01, ***p<0.001 vs. respective controls.

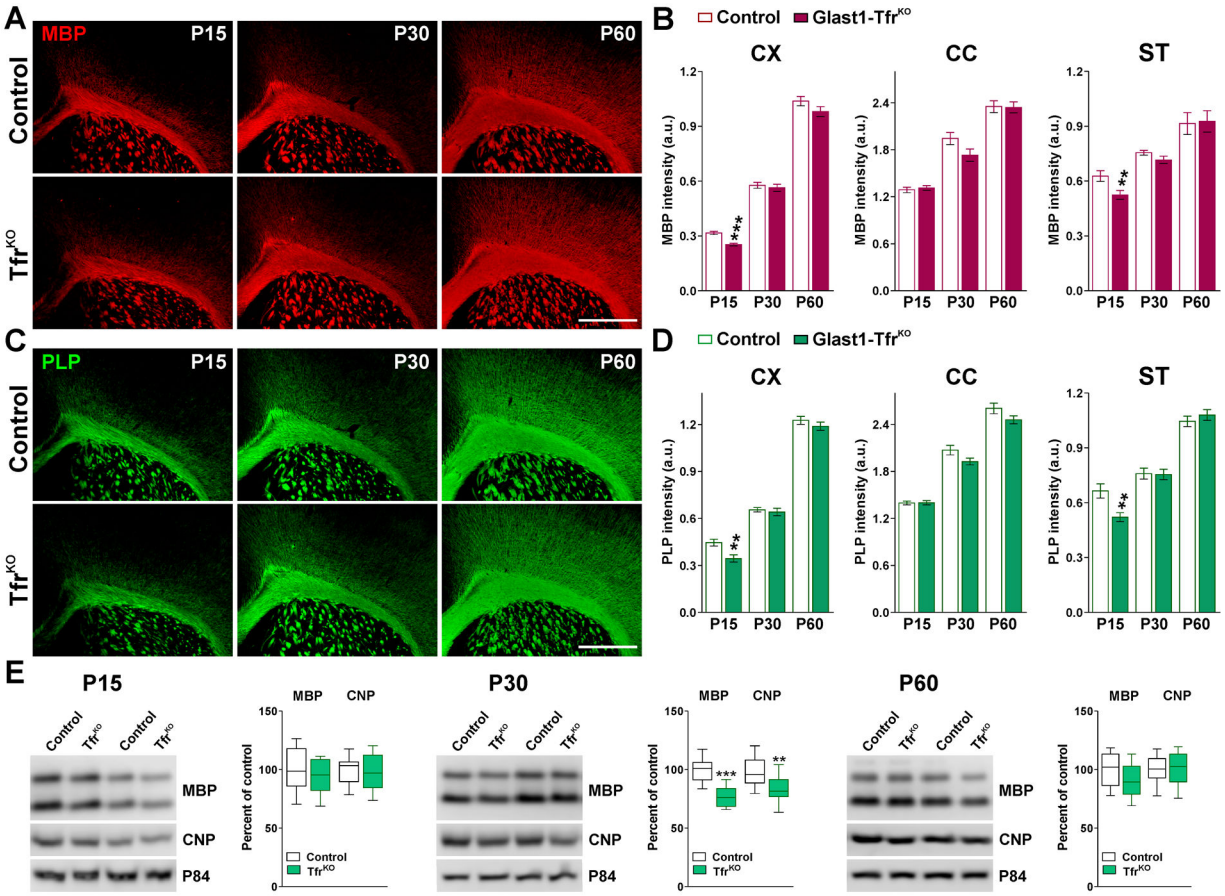

FIGURE 5: Myelin protein levels in the brain of Glast1-Tfr^{KO} animals.

(**A and C**) MBP and PLP immunostaining in the brain of control and Glast1-Tfr^{KO} mice at P15, P30 and P60. Scale bar=180μm. (**B and D**) Integrated fluorescence intensity for MBP and PLP in the CX, CC and ST. Values are expressed as mean ± SEM. **p<0.01, ***p<0.001 vs. respective controls. (**E**) Representative western blots for MBP and CNP in the CC of control and Glast1-Tfr^{KO} animals at P15, P30 and P60. P84 was used as the internal standard and box-and-whisker plots are showing means ± SD from 4 independent experiments. *p<0.05, **p<0.01, ***p<0.001 vs. respective controls.

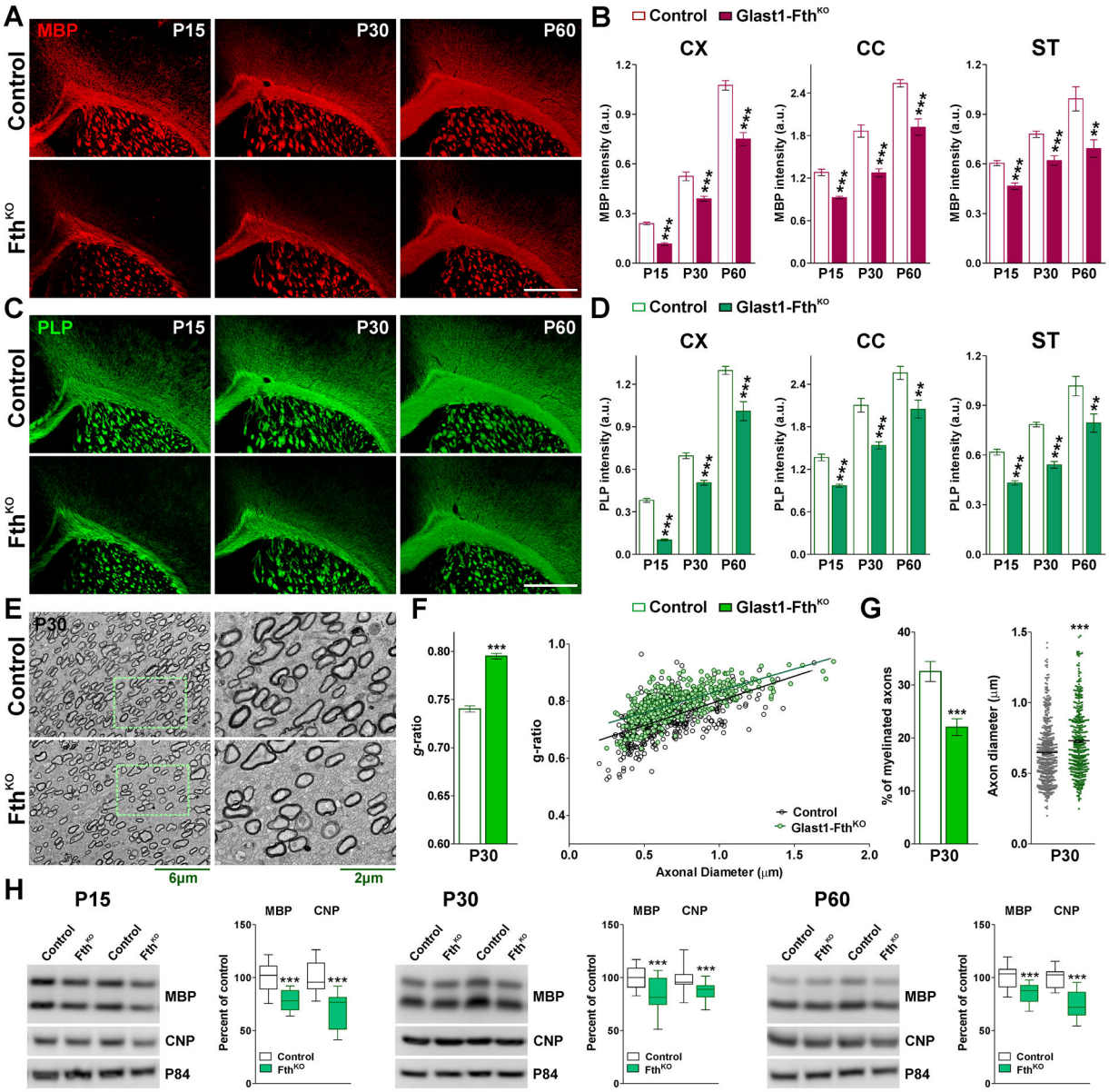

FIGURE 6: Postnatal myelination of the Glast1-Fth^{KO} brain.

(**A and C**) MBP and PLP immunostaining in the brain of control and Glast1-Fth^{KO} mice at P15, P30 and P60. Scale bar=180µm. (**B and D**) Integrated fluorescence intensity for MBP and PLP in the CX, CC and ST. Values are expressed as mean ± SEM. ***p<0.001 vs. respective controls. (**E**) Electron micrographs of axons in the CC of control and Glast1-Fth^{KO} mice at P30. Scale bar=6µm left panel; 2µm right panel. (**F**) Mean *g*-ratio values and scatter plot of *g*-ratio values of myelinated axons for the same experimental conditions. (**G**) Percentage of myelinated axons and mean axonal diameter of myelinated axons. Values are expressed as mean ± SEM. ***p<0.001 versus control. (**H**) Western blot analysis of MBP and CNP in the CC of control and Glast1-Fth^{KO} animals at P15, P30 and P60. P84 was used as the internal standard and box-and-whisker plots are showing means ± SD from 4 independent experiments. ***p<0.001 vs. respective controls.

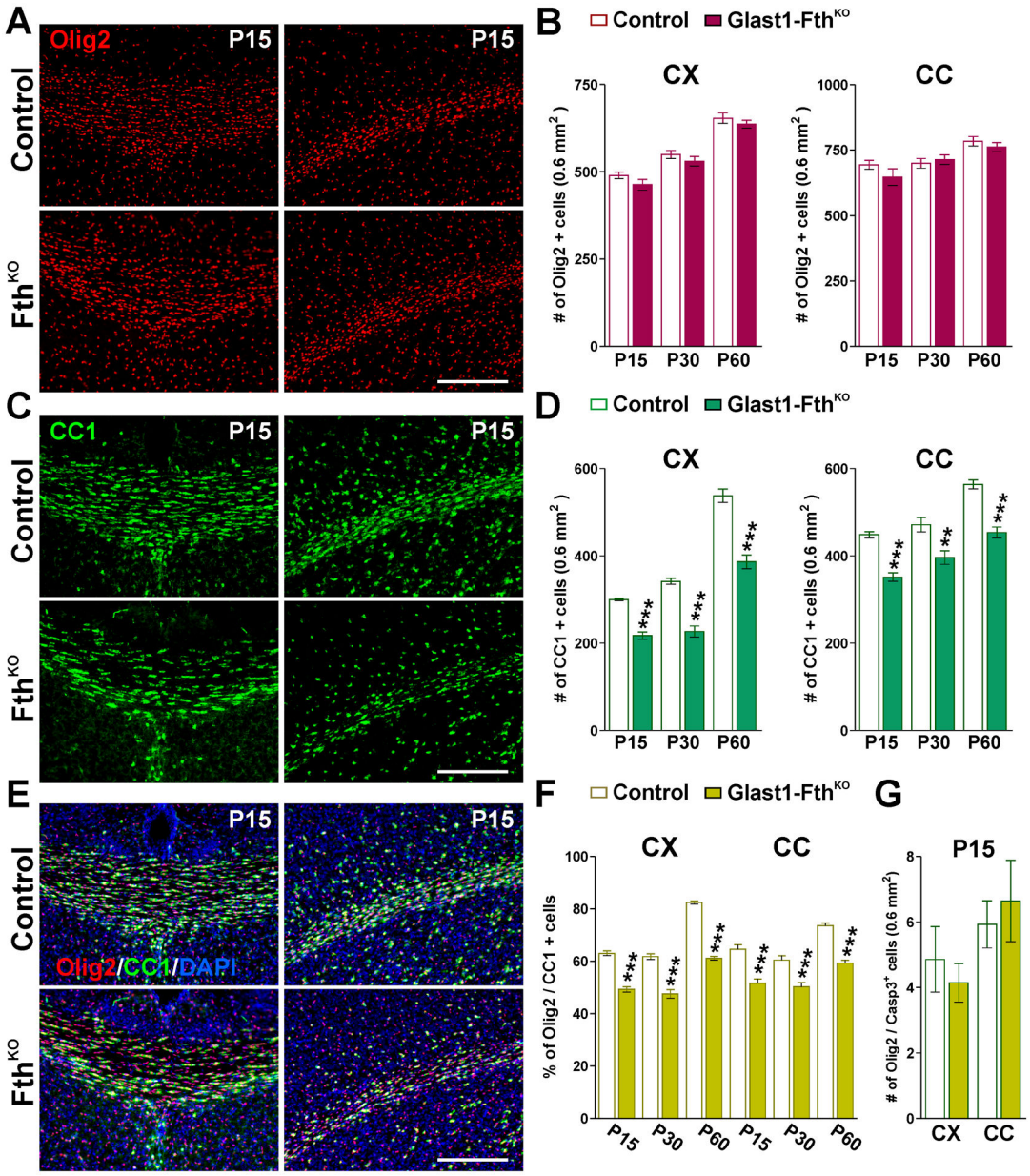

FIGURE 7: Oligodendrocyte quantities in young Glast1-Fth^{KO} mice.

(**A, C and E**) Brain coronal sections from control and Glast1-Fth^{KO} brains immunostained for Olig2 and CC1 at P15. Scale bar=90μm. (**B, D and F**) Total number of Olig2 and CC1-positive cells and percentage of Olig2/CC1 double-positive cells in the CX and CC at P15, P30 and P60. (**G**) Total number of Olig2/Casp-3 double-positive cells in the CX and CC at P15. Values are expressed as mean ± SEM. **p<0.01, ***p<0.001 vs. respective controls.

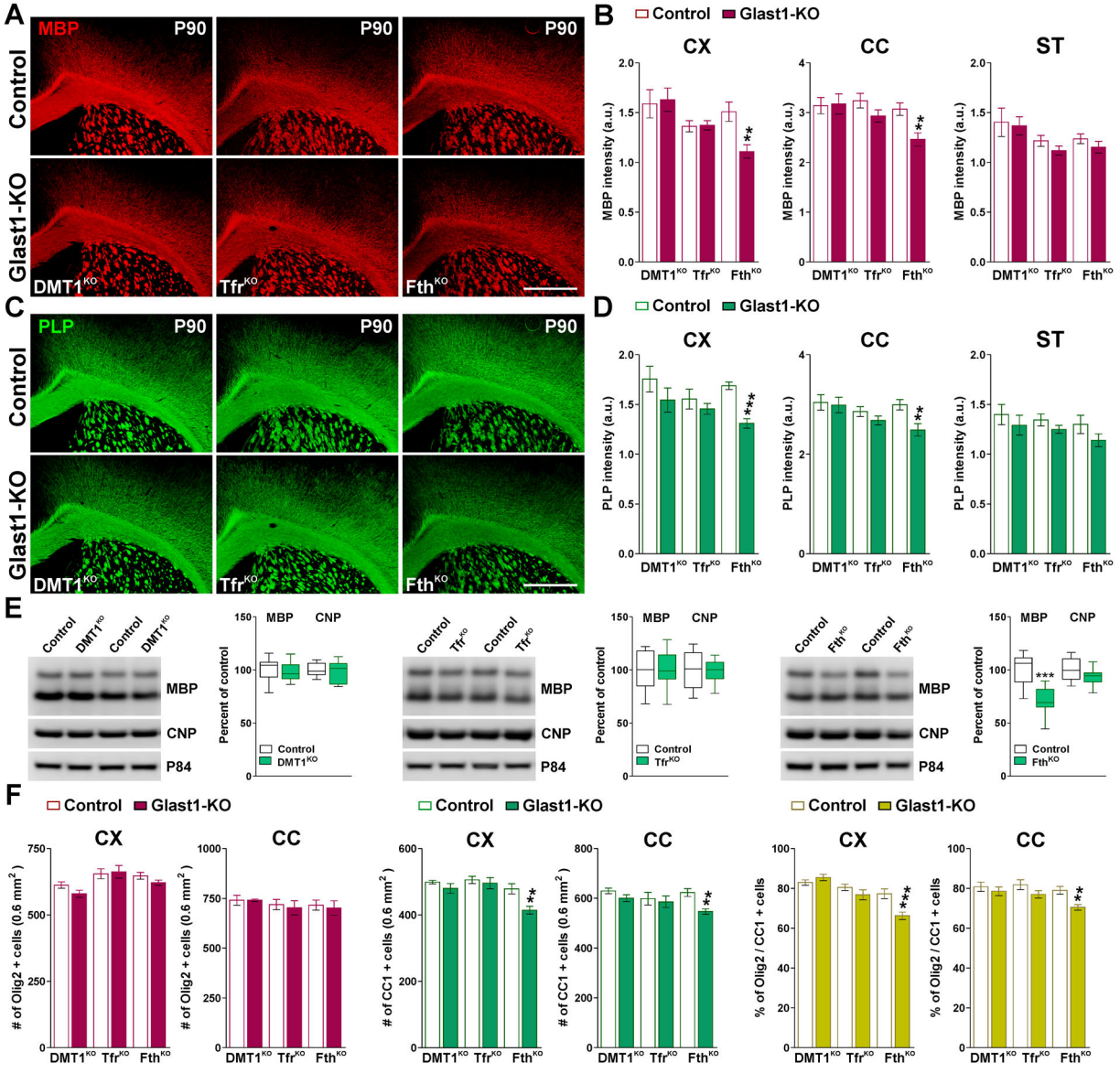

FIGURE 8: Myelin protein synthesis in adult Glast1-KO brains.

(**A and C**) MBP and PLP immunostaining in the brain of control and Glast1-KO mice at P90. Scale bar=180μm. (**B and D**) Integrated fluorescence intensity for MBP and PLP in the CX, CC and ST. Values are expressed as mean ± SEM. **p<0.01, ***p<0.001 vs. respective controls. (**E**) Western blot analysis for MBP and CNP in the CC of control and Glast1-KO animals at P90. P84 was used as the internal standard and box-and-whisker plots are showing means ± SD from 4 independent experiments. ***p<0.001 vs. respective controls. (**F**) Total number of Olig2 and CC1-positive cells and percentage of Olig2/CC1 double-positive cells in the CX and CC at P90. Values are expressed as mean ± SEM. **p<0.01, ***p<0.001 vs. respective controls.

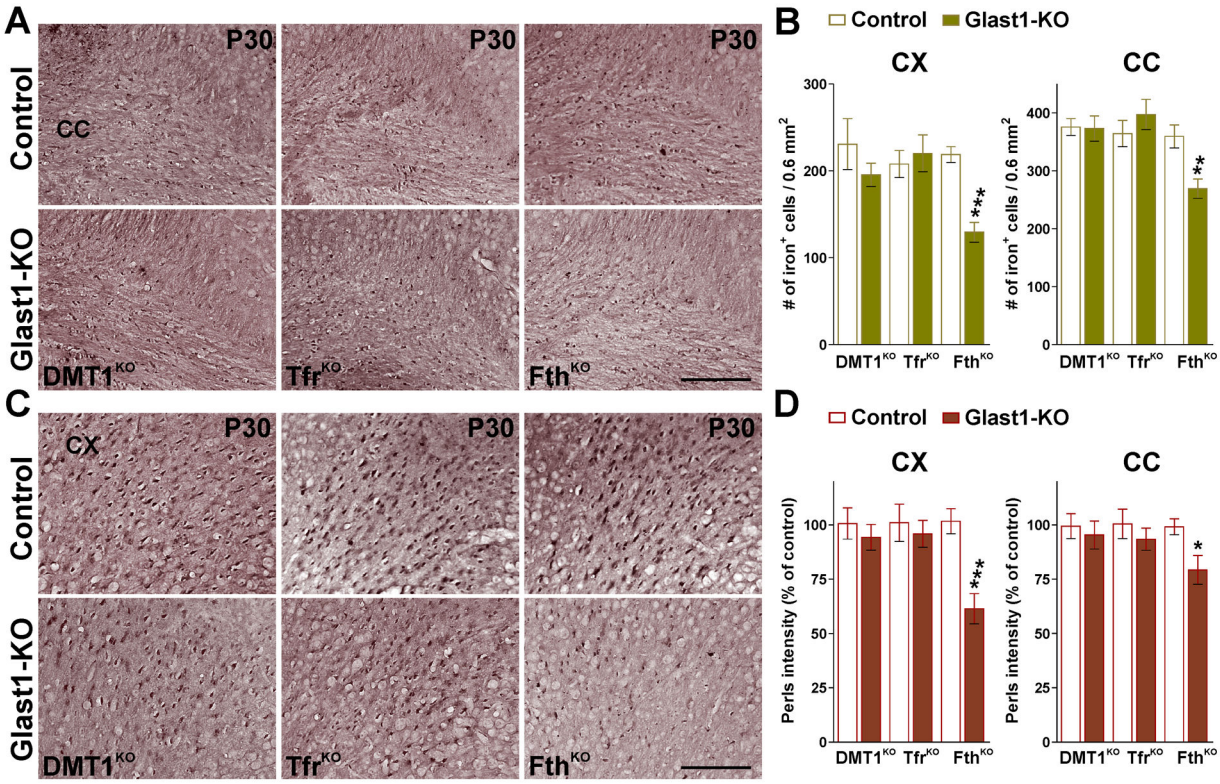

FIGURE 9: Perls staining in the Glast1-KO mice.

(**A and C**) Perls staining in brain coronal sections from control and Glast1-KO mice at P30. Scale bar=90μm. (**B and D**) Total number of Perls positive oligodendrocytes and average intensity staining per cell in the CX and CC at P30. Values are expressed as mean ± SEM. *p<0.05, **p<0.01, ***p<0.001 vs. respective controls.

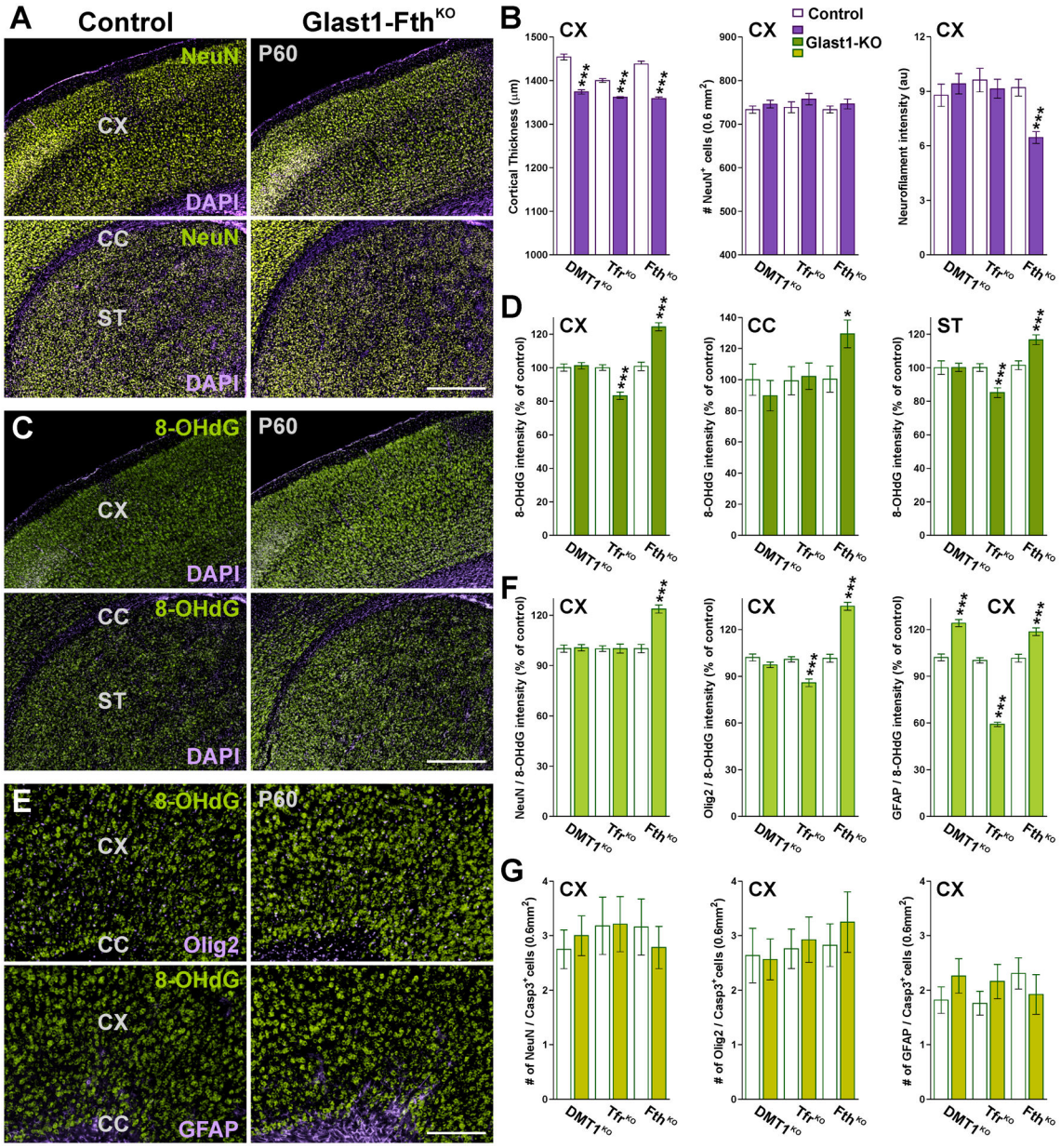

FIGURE 10: Neuronal densities, cell death and oxidative stress in Glast1-KO brains.

(**A, C and E**) Brain coronal sections from control and Glast1-Fth^{KO} brains immunostained for NeuN, Olig2, GFAP and 8-OHdG at P60. Scale bar=180µm upper panel; 90µm lower panels. (**B**) Cortical thickness, total number of NeuN-positive cells and integrated fluorescence intensity for the neurofilament L in the CX at P60. (**D**) Integrated fluorescence intensity of 8-OHdG in the CX, CC and ST at P60. (**F**) Integrated 8-OHdG fluorescence intensity in cortical NeuN-, Olig2- and GFAP-positive cells. (**G**) Total NeuN/, Olig2/ and GFAP/Casp-3 double-positive cells in the CX at P60. Values are expressed as mean ± SEM. *p<0.05, **p<0.01, ***p<0.001 vs. respective controls.

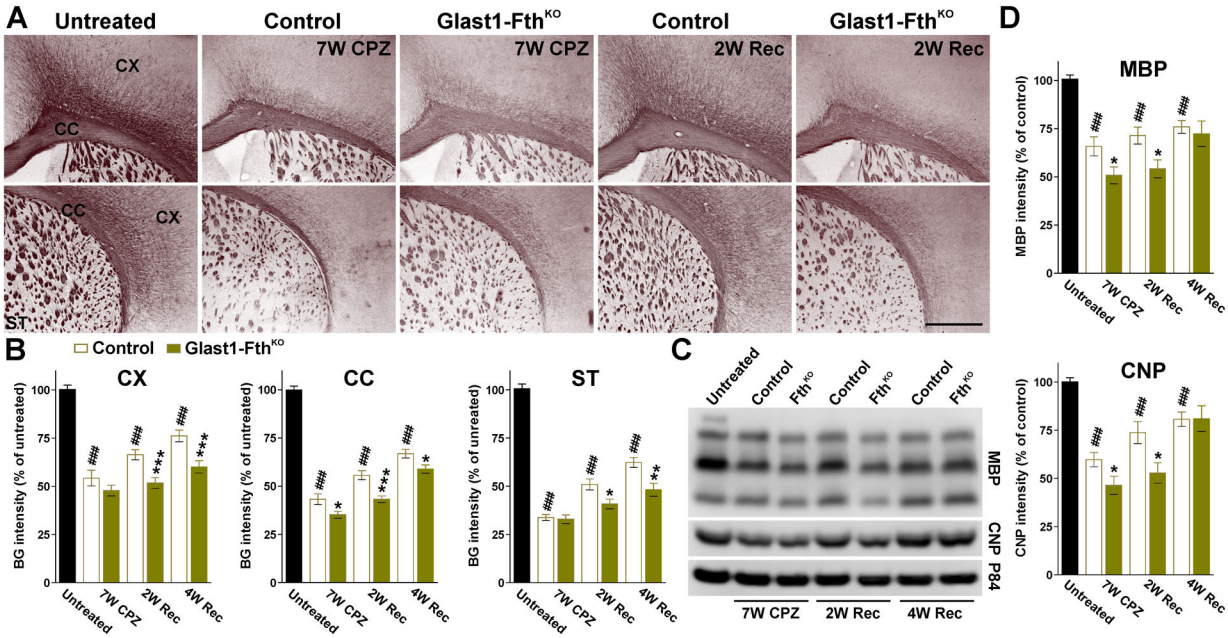

FIGURE 11: Black-gold staining in the remyelinating Glast1-Fth^{KO} brain.

(**A**) Black-gold staining in untreated, control and Glast1-Fth^{KO} mice at the end of the CPZ treatment (**7W CPZ**) and after 2 and 4 weeks of recovery (**2W and 4W Rec**). Scale bar=180μm. (**B**) Black-gold staining intensity in the CX, CC and ST of **untreated**, control and Glast1-Fth^{KO} mice at the end of the CPZ treatment (**7W CPZ**) and after 2 and 4 weeks of recovery (**2W and 4W Rec**). (**C and D**) Western blots for MBP and CNP in brain tissue comprised of the CX and CC. p84 was used as the internal standard and data from 4 independent experiments are summarized based on the relative spot intensities and plotted as percent of untreated mice. Values are expressed as mean ± SEM. ### p<0.001 versus untreated; * p<0.05, **p<0.01, ***p<0.001 versus control.

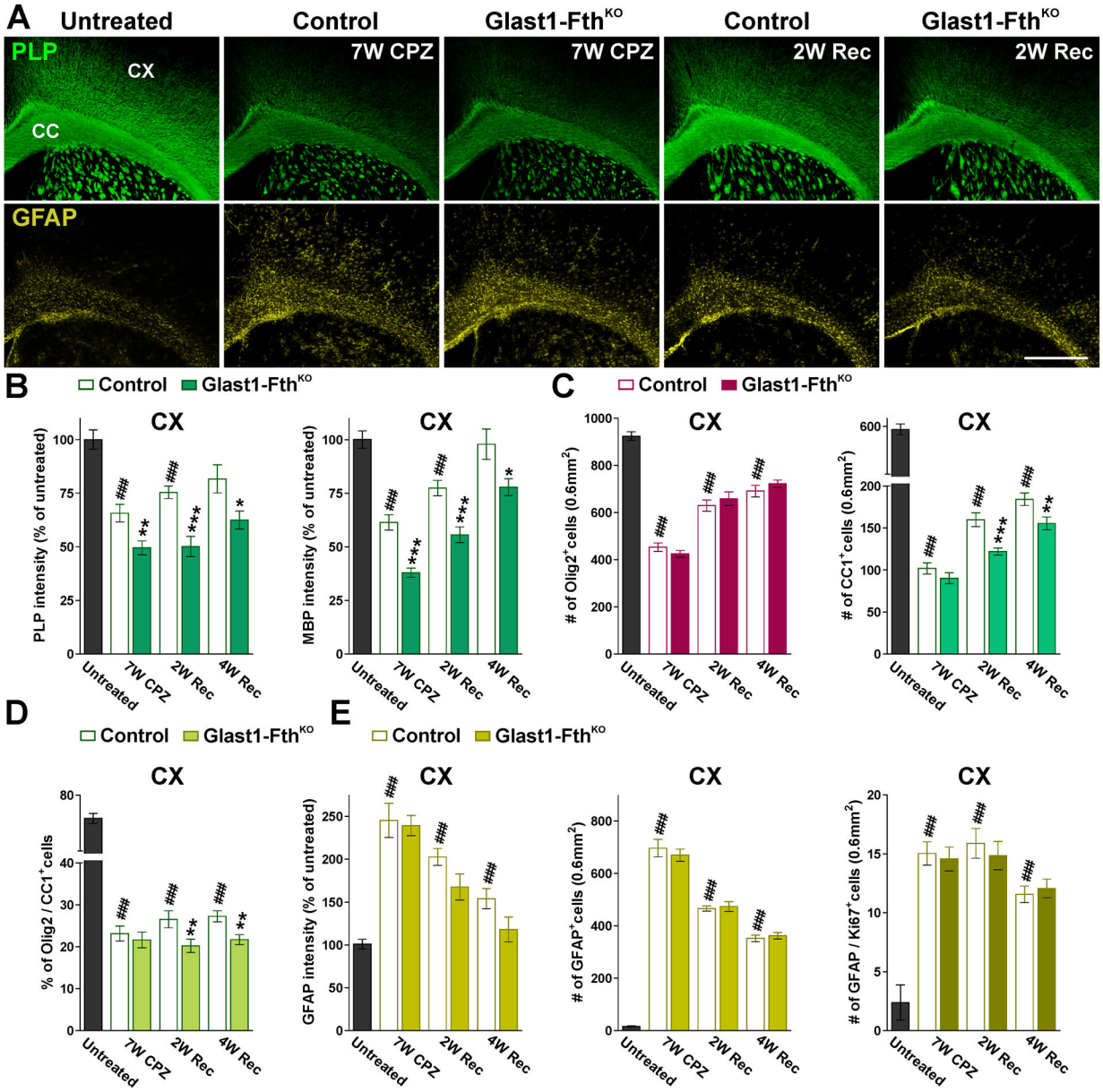

FIGURE 12: Remyelination and astrogliosis in the Glast1-Fth^{KO} brain.

(**A**) PLP and GFAP immunostaining in untreated, control and Glast1-Fth^{KO} mice at the end of the CPZ treatment (**7W CPZ**) and after 2 and 4 weeks of recovery (**2W and 4W Rec**). Scale bar=180μm. (**B and C**) PLP and MBP fluorescent intensity and total numbers of Olig2 and CC1-positive cells in the CX of untreated, control and Glast1-Fth^{KO} mice at the end of the CPZ treatment (**7W CPZ**) and after 2 and 4 weeks of recovery (**2W and 4W Rec**). (**D**) Percentage of Olig2/CC1 double-positive cells in the CX. (**E**) GFAP fluorescent intensity and total numbers of GFAP and GFAP/Ki67-positive cells in the CX under the same experimental conditions. Fluorescent intensity data is presented as percent of untreated mice. Values are expressed as mean ± SEM. ### p<0.001 versus untreated; *p<0.05, **p<0.01, ***p<0.001 vs. respective controls.